JOURNAL OF AIRCRAFT
Vol. 62, No. 2, March–April 2025

Exploration of a Low-Speed, Flapped, Slotted, Natural-Laminar-Flow Airfoil

Mark D. Maughmer,* Leonard P. Metkowski,† and Christopher J. Axten‡
The Pennsylvania State University, University Park, Pennsylvania 16802
and
Dan M. Somers§
Airfoils, Incorporated, Port Matilda, Pennsylvania 16870

https://doi.org/10.2514/1.C037802

A 12.91%-thick, flapped, slotted, natural-laminar-flow (SNLF) airfoil, the S702, intended for a low-speed, fixed-wing aircraft, has been designed, analyzed theoretically, and verified experimentally in The Pennsylvania State University Low-Speed, Low-Turbulence Wind Tunnel. The two primary objectives of high maximum lift that is insensitive to roughness and low-profile drag have been achieved. The use of a simple flap for manipulation of the low-drag region and control purposes was also explored and found to provide the desired characteristics. The airfoil exhibits a sharp stall that is less abrupt than the stalls of earlier SNLF airfoils, which meets the design objective. The constraint on the pitching moment has been satisfied. Comparisons of the theoretical and experimental results show reasonably good agreement overall, given the complexity of the configuration.

Nomenclature

C_p	=	pressure coefficient; $(p_l - p_\infty)/q_\infty$
c	=	airfoil chord, in.
c_d	=	section profile-drag coefficient
c_l	=	section lift coefficient
c_m	=	section pitching-moment coefficient about quarter-chord point
M	=	freestream Mach number
p	=	static pressure, lb/ft^2
q	=	dynamic pressure, lb/ft^2
Re_c	=	Reynolds number based on freestream conditions and airfoil chord
x	=	airfoil abscissa, in.
α	=	angle of attack relative to x axis, deg
δ_f	=	flap deflection, deg

Subscripts

l	=	local point on airfoil
max	=	maximum
S	=	separation
T	=	transition
∞	=	freestream conditions

I. Introduction

THE wing profile drag is the largest contributor to the total aircraft drag at cruise conditions for most aircraft because of the generally low lift coefficients and correspondingly low induced drag. The wing profile drag contributes about one third of the total drag for transport aircraft. As the aircraft size decreases from transport through regional to business jets and other general aviation (GA) aircraft and finally unmanned aerial vehicles (UAVs) and sailplanes, the percentage of the total aircraft drag due to the wing profile drag generally increases to approximately one half, primarily because the relative wing area increases and the chord Reynolds number decreases.

To minimize wing profile drag, the figure of merit (FOM), given by

$$\text{FOM} = \frac{c_{l,\max}}{c_{d,\text{cruise}}} \tag{1}$$

where $c_{l,\max}$ is the section maximum lift coefficient and $c_{d,\text{cruise}}$, the cruise section profile-drag coefficient, should be maximized [1]. It should be noted that the figure of merit is expressed in terms of section (airfoil) characteristics and not aircraft characteristics. It is most applicable to aircraft having their wing area determined by a minimum-speed requirement (usually landing speed). The figure of merit can be interpreted such that if the wing area is set by a low-speed requirement, for example, landing speed, then a higher lift coefficient will generally lead to less wing area. As the total profile drag depends on the product of the profile-drag coefficient and the wing area, less wing area results in less profile drag. Likewise, the wing profile drag can also be reduced if a lower section profile-drag coefficient is achieved. This figure of merit applies to almost all aircraft types. For those aircraft having their wing area determined by a fuel-volume requirement (e.g., business jets), reducing the section profile-drag coefficient is even more beneficial.

Three approaches have become accepted for the reduction of wing profile drag. One approach is to employ a high-lift system (e.g., leading-edge slat plus double- or triple-slotted, Fowler flap) to achieve a higher maximum lift coefficient [2]. This approach has several disadvantages. Almost no laminar flow is possible because of the disturbances introduced by the slat, which results in a high section profile-drag coefficient. The maximum lift coefficient is limited to about 4, which limits the reduction in wing area. High-lift systems are complex, both mechanically and structurally, resulting in higher weight and cost. This approach can provide a maximum wing profile-drag reduction of about 50% compared to a conventional, turbulent-flow wing with no high-lift system and has been adopted for all current transport aircraft. Active high-lift systems (e.g., blown flaps and circulation control) have demonstrated very high lift coefficients, but the cost, complexity, and potentially disastrous failure modes have prevented their adoption for production aircraft.

A second approach is to employ a natural-laminar-flow (NLF) airfoil to achieve a lower profile-drag coefficient [3]. By appropriate airfoil shaping, extensive (greater than 30% chord) laminar flow can

Presented as Paper 2023-4313 at the AIAA Aviation Forum 2023, San Diego, CA, June 23–27, 2023; received 12 January 2024; accepted for publication 30 September 2024; published online 20 December 2024.

*Professor, Department of Aerospace Engineering, 308 ECoRE Building; mdm@psu.edu. Fellow AIAA.
†Graduate Assistant, Department of Aerospace Engineering; currently Computational Fluid Dynamics Engineer in the Systems Engineering Group, Axient Corporation, Catonsville, Maryland, 22485.
‡Postdoctoral Scholar, Department of Aerospace Engineering, 229 Hammond Building; cja5217@psu.edu. Member AIAA.
§President, 122 Rose Drive.

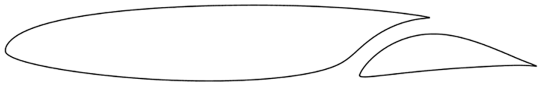

Fig. 1 The S414 SNLF airfoil [8].

be achieved on both the upper and lower wing surfaces. The extent of laminar flow is limited to about 70% chord by the pressure-recovery gradient along the aft portion of the airfoil and by leading-edge sweep. The recovery gradient becomes steeper as the extent of the favorable gradient along the forward portion of the airfoil increases, eventually reaching a limit beyond which trailing-edge separation occurs, resulting in a lower maximum lift coefficient and, correspondingly, a lower figure of merit. Leading-edge sweep restricts the extent of laminar flow because it introduces crossflow instabilities that lead to transition. For aircraft able to take advantage of laminar flow, that is, designs not having a large amount of sweep or that operate at very high Reynolds numbers, the implementation of NLF can also provide a wing profile-drag reduction of about 50% compared to a conventional, turbulent-flow wing. Consequently, NLF airfoils have been employed on many GA aircraft, including business jets, as well as UAVs and all sailplanes. It does, however, require more stringent construction techniques.

A third approach is to employ a laminar-flow-control (LFC) airfoil to achieve a lower profile-drag coefficient [4–6]. By incorporating suction through porous or slotted, wing skins, 100%-chord laminar flow can be achieved on both the upper and lower wing surfaces. LFC systems are very complex, mechanically, structurally, and operationally, resulting in higher weight and cost. This approach can provide a wing profile-drag reduction of about 75% compared to a conventional, turbulent-flow wing but has yet to be adopted for any production aircraft.

For the present effort, a new approach, called a slotted, natural-laminar-flow (SNLF) airfoil, is employed [7]. An earlier design, the S414 airfoil, is shown in Fig. 1 [8]. The SNLF airfoil concept is similar in nature to the slotted, supercritical airfoil concept in that it employs a slot to allow a pressure recovery that would not be possible for a single-element airfoil [9].

II. Airfoil Design

A. Objectives and Constraints

The SNLF airfoil concept incorporates passive laminar flow control with a multi-element airfoil. While common for high-lift configurations, multi-element airfoils have been explored for cruise as well, such as the slotted, supercritical airfoil concept noted; however, the SNLF concept is unique in using the configuration to create favorable pressure gradients to promote laminar flow [7]. The pressure distribution over the aft element allows the fore element to recover to pressures lower than freestream. This enables the fore element to maintain favorable pressure gradients over the entirety of the upper and lower surfaces, thus promoting laminar flow over that element. The aft element operates with mostly adverse pressure gradients; however, due to the lower Reynolds numbers and the magnitude of the adverse pressure gradients, the flow over the aft element is generally laminar aside from roughly the aft half of its upper surface.

The design specifications for this new airfoil are directed toward the goal of an airfoil that can be fully tested in a low-speed facility but can also have meaningful applications for a variety of low-speed aircraft. A second goal is to explore the incorporation of a simple flap on the aft element. The flap is intended to shift the low-drag range to lower and higher lift coefficients with negative and positive deflections, respectively. The deflections also allow the evaluation of the flap as a control surface.

The airfoil design specifications are presented in Table 1. Two primary objectives are evident from these specifications. The first objective is to achieve a maximum lift coefficient, with positive flap deflection, of at least 2.0 for a Reynolds number of 0.29×10^6 to 0.91×10^6. This objective is considered ambitious, primarily because of the low operational Reynolds numbers. A requirement related to this objective is that the maximum lift coefficient does not decrease significantly with transition fixed near the leading edge on all surfaces. In addition, the airfoil should exhibit stall characteristics that are less abrupt than those of the two earlier SNLF airfoils investigated experimentally, the S103 [10] and the S414 [8]. The second objective is to obtain low profile-drag coefficients with a negative flap deflection over the ranges of lift coefficients and Reynolds numbers shown in Table 1. The root and tip Reynolds numbers represent the conditions for a nominal double-taper wing of a high-performance sailplane. The pitching-moment coefficient with no flap deflection at the lower limit of the low-drag range was constrained to −0.20 for Reynolds numbers from 0.80×10^6 to 2.50×10^6. There was no constraint on the airfoil thickness.

Table 1 Airfoil design specifications

Parameter	Value	Reynolds number, Re_c Tip	Reynolds number, Re_c Root	Priority
Maximum lift coefficient $c_{l,\max}$ with positive flap deflection	≥2.00	0.29×10^6	0.91×10^6	High
Lower limit of low-drag, lift-coefficient range, $c_{l,\text{ll}}$, without/with negative flap deflection	0.30 0.20	0.80×10^6 0.94×10^6	2.50×10^6 3.00×10^6	High
Upper limit of low-drag, lift-coefficient range, $c_{l,\text{ul}}$, without/with negative flap deflection	0.60 0.30	0.55×10^6 0.80×10^6	1.70×10^6 2.50×10^6	High
Pitching-moment coefficient c_m at $c_{l,\text{ll}}$ without flap deflection	≥ -0.20	0.80×10^6	2.50×10^6	Medium

Additional objectives and constraints:
Incompressible ($M \approx 0$).
Maximum lift coefficient $c_{l,\max}$ independent of leading-edge roughness.
Stall characteristics less abrupt than earlier SNLF airfoils.
Simple flap on aft element.

B. Philosophy

Given the above objectives and constraints, certain characteristics of the design are apparent. The sketch presented in Fig. 2 illustrates a hypothetical drag polar that meets the goals for this design. Point A is the lower limit of the low-drag, lift-coefficient range, and point B, the upper limit. The profile-drag coefficient increases very rapidly outside the low-drag range because boundary-layer transition moves quickly toward the leading edge with increasing (or decreasing) lift coefficient. This feature results in a leading edge that produces a suction peak at higher lift coefficients, which ensures that transition on the upper surface will occur near the leading edge. Thus, the

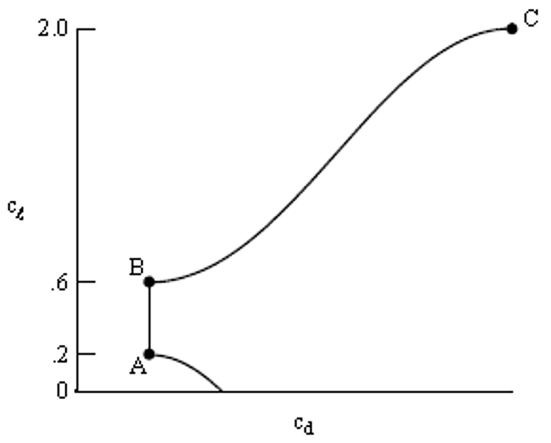

Fig. 2 Sketch of a drag polar that meets the design goals.

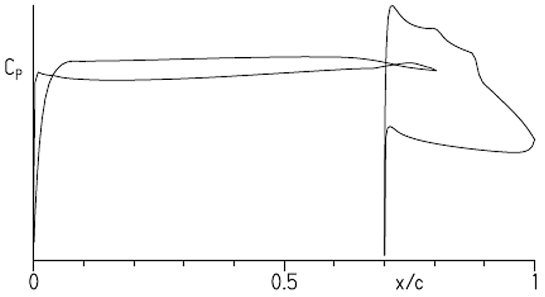

Fig. 3 Pressure distribution for two-element airfoil.

maximum lift coefficient, point C, occurs with turbulent flow along the entire upper surface and, therefore, should be insensitive to roughness at the leading edge.

A two-element airfoil concept is used to meet the design objectives. Several features of the design are illustrated in the sketch presented in Fig. 3. The pressure gradient over the upper surface of the fore element near the leading edge is very favorable to restrain the pressure peak at high angles of attack. The pressure gradient then becomes essentially neutral. About 15% chord forward of the trailing edge of the fore element, an adverse pressure gradient is introduced that is not so steep as to cause transition within the low-drag range but still provides a "separation ramp." This feature helps achieve docile stall characteristics [11].

Along the lower surface of the fore element, the pressure gradient is initially adverse, then neutral, and then increasingly favorable. Transition is imminent over the entire lower surface of the fore element [12]. The specific pressure gradients employed along the forward portion of the lower surface increase the loading in the leading-edge region while maintaining low drag at the lower lift coefficients. The forward loading serves to decrease the magnitude of the pitching-moment coefficient while contributing to the achievement of a high maximum lift coefficient.

Because the aft element eliminates the requirement that the pressure at the trailing edge of the fore element recover to freestream [13], the neutral pressure gradient along the upper surface and the favorable gradient along the lower surface can extend farther aft. For the SNLF airfoil concept, these gradients extend along both surfaces of the fore element to near its trailing edge. Thus, the fore element can be entirely laminar. The aft element then provides the necessary recovery to freestream pressure. Because the wake of the fore element does not impinge on the aft element and because of its lower Reynolds number, the aft element can also achieve significant extents of laminar flow, even without favorable pressure gradients.

The SNLF airfoil concept allows the extent of natural laminar flow to be increased beyond the limit for single-element NLF airfoils previously discussed. Thus, the concept allows lower section profile-drag coefficients to be achieved without having to resort to the complexity and cost of laminar flow control. The concept also achieves a high maximum lift coefficient without variable geometry (i.e., the aft element need not be deflected), although the simple flap on the aft element can be used to augment the maximum lift. The aft-element flap is also capable of shifting the low-drag, lift-coefficient range, effectively widening the range. The SNLF airfoil shape is not radically different from conventional airfoil shapes, no more so than conventional NLF airfoil shapes are from conventional turbulent-flow airfoils. Unlike conventional airfoils with slotted flaps, however, the SNLF airfoil has no nested configuration; the slot between the fore and aft elements is always open.

C. Execution

The Eppler Airfoil Design and Analysis Code [14,15], a single-element code, was used to design the initial fore- and aft-element shapes. The MSES code [16], a multi-element Euler solver, was used to refine the fore-element shape in the two-element configuration, particularly along the lower surface in the slot region. MSES was run with the mesh generated by default, and the boundary conditions were determined by the maximum lift coefficient as suggested in the MSES user's guide (the low Mach number had no influence on the boundaries).

Fig. 4 S702 airfoil model and flap settings tested.

The airfoil is designated the S702 and presented in Fig. 4. It should be noted that the chord line does not intersect the trailing edge of the aft element, which is an artifact of the design process. The maximum thickness of the airfoil is 12.91% chord.

Coordinates for the S702 airfoil are available from Airfoils, Incorporated, Port Matilda, PA.

D. Theoretical Procedure

The theoretical results are predicted using the MSES code [16]. A critical amplification factor of 9 was specified for the computations. It should be noted that this method does not model the effect of Görtler instabilities on the laminar boundary layer [17]; however, an evaluation of this effect was performed and indicated that these instabilities will not lead to transition in the concave region of the lower surface of the fore element for the Reynolds numbers of concern [18].

Because the freestream Mach number for all wind-tunnel test conditions did not exceed 0.16, the flow can be considered nearly incompressible, which allows the fast, subcritical flow solver of the MSES code to be used.

III. Experimental Procedure

A. Wind Tunnel, Model, and Data-Acquisition System

The Penn State University Low-Speed, Low-Turbulence Wind Tunnel is a closed-throat, single-return atmospheric facility [19]. The test section is rectangular, 3.3 ft high and 4.4 ft wide, with filleted corners. The maximum test-section speed is 220 ft/s. Airfoil models are mounted vertically in the test section and attached to computer-controlled turntables that allow the angle of attack to be set. The turntables are flush with the floor and ceiling and rotate with the model. The axis of rotation is at the 42%-chord point for this model. The gaps between the model and the turntables are sealed to prevent leaks. At a velocity of 150 ft/s, the flow angularity in the test section is everywhere below 0.25 deg, the mean velocity variation is below 0.2%, and the turbulence intensity is less than 0.045%. The flow quality of the Penn State LSLTT has been measured and documented [19].

The aluminum model for this test was fabricated by Advanced Technologies, Incorporated, Newport News, VA, using a numerically controlled milling machine. The model had a chord of 18.0 in. and a span of 42.5 in. and, thus, extended through both turntables. The finite-thickness, trailing-edge geometries were designed to simulate typical composite construction. The hinge point for the simple flap on the aft element was located at $x/c = 0.9001$, $z/c = -0.0114$ and thus coincided with the lower-surface contour to simulate the hinge design of Ref. [20]. The region on the upper surface of the aft element encompassing the hinge point was covered by a plastic film secured to the aluminum by adhesive. Some discontinuities in the surface due to the plastic film, including small steps, are apparent in some of the measured pressure distributions. Upper- and lower-surface orifices were located to one side of midspan at the staggered positions. All the orifices were 0.020 in. in diameter with their axes perpendicular to the surface. The surfaces of the model were sanded to ensure an aerodynamically smooth finish. The measured model contour was within 0.005 in. of the prescribed shape. The airfoil coordinates are available from Airfoils, Incorporated.

Drag measurements are obtained using a wake-traversing, Pitot-static pressure probe mounted from the ceiling of the tunnel and positioned 21.6 in. from the top wall and 19.1 in. from the bottom wall (i.e., roughly midspan). The outer diameter of the probe is 0.25 in. The tip of the probe is located 0.78 chord downstream of the model trailing edge. A traversing mechanism incrementally positions the probe across the wake with survey increments of 0.05 in., and

the probe automatically aligns with the local wake-center streamline as the angle of attack changes. The basic wind-tunnel pressures are measured using pressure-sensing diaphragm transducers, and pressure measurements on the model are made via an automatic pressure-scanning system. Data are obtained and recorded with an electronic data-acquisition system.

B. Experimental Methods

The pressures measured on the model were reduced to standard pressure coefficients and numerically integrated to obtain section normal-force and chord-force coefficients and section pitching-moment coefficients about the quarter-chord point. Section profile-drag coefficients were computed from the wake total and static pressures by the method of Ref. [21]. At most poststall angles of attack, however, wake surveys were not performed, and the profile-drag coefficients were computed from the normal- and chord-force coefficients. Standard, low-speed, wind-tunnel boundary corrections have been applied to the data [22]. The wake-survey-probe total-pressure-tube displacement correction has been taken into account [21].

The uncertainty of a measured force or moment coefficient depends on the operating conditions and generally increases with increasing angle of attack [23]. At higher lift, for which the uncertainty is greatest, the measured lift coefficients have an uncertainty of $\Delta c_l = \pm 0.005$, and the pitching-moment coefficients have an uncertainty of $\Delta c_m = \pm 0.002$. The uncertainty of the drag coefficients measured in the low-drag range is $\Delta c_d = \pm 0.00005$ (0.5 drag counts), increasing to $\Delta c_d = \pm 0.00015$ (1.5 drag counts) as the angle of attack approaches stall.

Four configurations were tested, comprising flap deflections of 0°, −2°, 5°, and 10°, as depicted in Fig. 4. The model was tested at Reynolds numbers based on airfoil chord of 0.50×10^6, 0.70×10^6, 1.00×10^6, and 1.50×10^6 with transition free (smooth). In addition, measurements were also taken with transition fixed (forced), and although these data are not included here, a complete set is presented in Ref. [24].

All the polar data were obtained by starting near the middle of the low-drag, lift-coefficient range, and then the angle of attack was decreased to that near zero lift. The angle of attack was then increased from the middle of the low-drag range to poststall values. This procedure is intended to alleviate any hysteresis in the transition location, especially around the limits of the low-drag range.

For several test runs, the model surfaces were coated with oil to determine the location as well as the nature of the boundary-layer transition from laminar to turbulent flow and the location of turbulent separation [25]. Oil-flow visualization was also used to verify the two-dimensionality of the flow. In addition, acoustic measurements were used to confirm the transition locations [4].

IV. Experimental Results

A. Pressure Distributions

The pressure distributions at various angles of attack with a flap deflection of 0° for a Reynolds number of 1.00×10^6 and a Mach number of 0.10 with transition free are shown in Figs. 5a–5c. From Fig. 5a, it can be observed that as the angle of attack is increased from −7.13°, the circulation on the aft element increases. At nearly all higher angles of attack, because the flowfield of the aft element is constrained by that of the fore element, the aft element pressure distribution is essentially constant. As the angle of attack is increased from −4.08°, the initially adverse pressure gradient on the lower surface of the fore element becomes nearly neutral to the trailing edge of the fore element, including in the region of the slot, indicating that the flow along the entire lower surface may be laminar, which was later confirmed by acoustic measurements. At an angle of attack of −1.02°, the pressure gradient on the upper surface of the fore element is initially very favorable but quickly becomes essentially neutral to about 65% chord. The shallow, adverse pressure gradient aft of that point is not unfavorable enough to cause boundary-layer transition, which was later confirmed by acoustic and oil-flow measurements. At an angle of attack of 2.03°, presented in Fig. 5b, an indication of a laminar separation bubble on the upper surface of the aft element around its midchord can be observed in the pressure distribution. The bubble seems to disappear as the angle of attack is increased, possibly because of the influence of turbulent flow coming from the upper surface of the fore element, as confirmed by acoustic and oil-flow measurements. At an angle of attack of 8.13°, a laminar separation bubble is evident on the upper surface of the fore element around 8% chord. As the angle of attack is increased further, as can be observed in Fig. 5c, the bubble on the upper surface of the fore element migrates forward, and the bubble, again evident on the upper surface of the aft element, becomes more pronounced and migrates forward. As the angle of attack increases, turbulent, trailing-edge separation

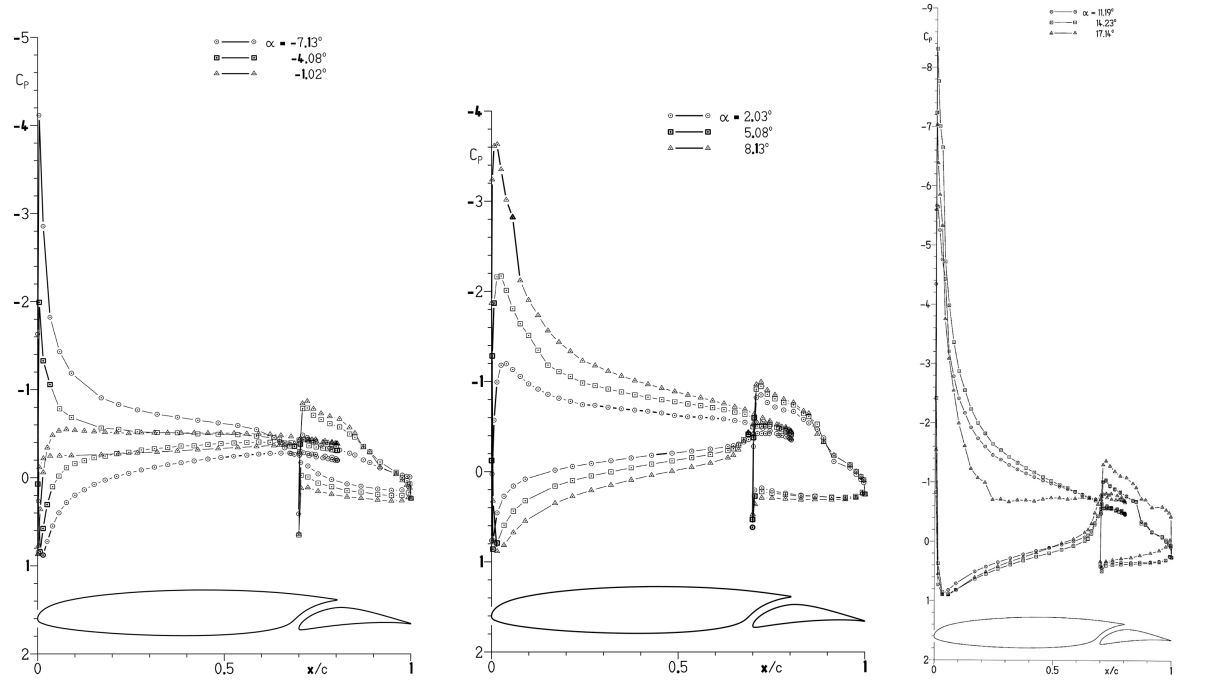

a) α = -7.13°, -4.08°, and -1.02° b) α = 2.03°, 5.08°, and 8.13° c) α = 11.19°, 14.23°, and 17.14°

Fig. 5 a–c) Pressure distributions with $\delta_f = 0°$ for $Re_c = 1.00 \times 10^6$ and $M = 0.10$ with transition free.

occurs on the upper surface of the fore element and moves forward. The pressure distribution on the aft element changes dramatically because of its higher apparent angle of attack, although no trailing-edge separation is evident. As the angle of attack is increased to 17.14°, the separation point moves forward on the fore element, but the leading-edge pressure peak does not collapse, demonstrating that leading-edge stall does not occur.

Additional pressure distributions at various angles of attack with flap deflections of −2°, 5°, and 10° for a Reynolds number of 1.00×10^6 and a Mach number of 0.10 with transition free are included in Ref. [24]. The behavior of the pressure distributions for the −2° flap deflection is very similar to that with a flap deflection of 0° because the small, negative flap deflection has only a minor influence on the overall pressure distributions. For the 5° flap deflection, the increased circulation on the aft element induces higher velocities on the lower surface of the fore element in the slot region. In other respects, the behavior of the pressure distributions is similar to that with flap deflections of 0° and −2°.

The pressure distributions at various angles of attack with a flap deflection of 10° for a Reynolds number of 1.00×10^6 and a Mach number of 0.10 are similar to the other cases shown. Again, the increased circulation on the aft element due to the positive flap deflection induces even higher velocities on the lower surface of the fore element in the slot region. Despite the steep, aft pressure recovery on the upper surface of the aft element, trailing-edge separation does not occur, even after trailing-edge separation occurs on the fore element.

The effect of flap deflection on the pressure distribution at an angle of attack of −1.02° for a Reynolds number of 1.00×10^6 and a Mach number of 0.10 with transition free is summarized in Fig. 6. The increase in circulation on the fore and aft elements with flap deflection is evident.

B. Section Characteristics

1. *Reynolds Number Effects*

The effects of Reynolds number on the section characteristics with a flap deflection of 0° and transition free are summarized in Fig. 7 for a Reynolds number of 0.50×10^6 to 1.5×10^6. The stall characteristics are sharp, but the abrupt break of earlier SNLF airfoils [8,10] is mitigated slightly, which does meet the design objective. For a Reynolds number of 1.50×10^6 and a Mach number of 0.15, the lower limit of the low-drag, lift-coefficient range is about 0.17, which is lower than the design objective of 0.30. The upper limit is about 0.50, which is also lower than the objective of 0.60. The pitching-moment coefficient at a lift coefficient of about 0.3 is −0.12°, which is smaller in magnitude than the design constraint of −0.20.

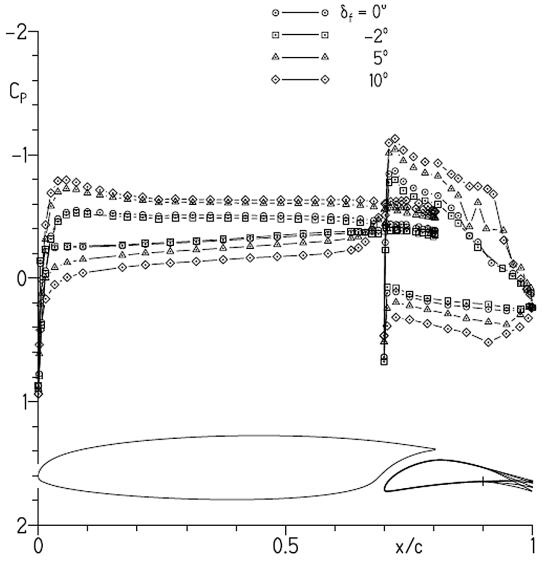

Fig. 6 Effect of flap deflection on pressure distribution at $\alpha = 1.02°$ for $Re_c = 1.00 \times 10^6$ and $M = 0.10$ with transition free.

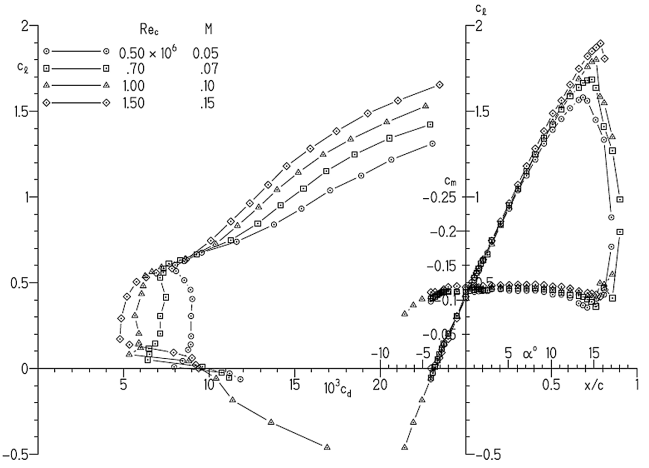

Fig. 7 Effects of Reynolds number on section characteristics with $\delta_f = 0°$ and transition free.

The lower drag at the upper and lower corners of the low-drag range of the drag polar for a Reynolds number of 0.50×10^6 and, to a lesser extent, the Reynolds numbers of 0.70×10^6 and 1.00×10^6 is probably the result of an interaction between the wake of the fore element and the laminar separation bubble on the upper surface of the aft element [8]. As the angle of attack approaches the lower or upper limit of the low-drag range, transition occurs near the trailing edge of the fore element. The resulting turbulence probably alleviates the laminar separation bubble on the upper surface of the aft element, reducing the drag.

A notable characteristic, unlike that of most single-element airfoils, is the large increase in the magnitude of the negative pitching-moment coefficient that happens at stall. This behavior occurs because the flow on the aft element remains attached, even poststall, as can be observed in Fig. 5.

In general, the maximum lift coefficient, the lower limit of the low-drag range, the magnitude of the pitching-moment coefficients, and the lift-curve slope at higher lift coefficients increase with increasing Reynolds number. In addition, the stall characteristics generally become sharper. The profile-drag coefficients and the upper limit of the low-drag range decrease with increasing Reynolds number. All these effects are typical.

2. *Effects of Flap Deflection*

The section characteristics with flap deflections of −2°, 0°, 5°, and 10° with transition free are shown in Fig. 8. For a Reynolds number of

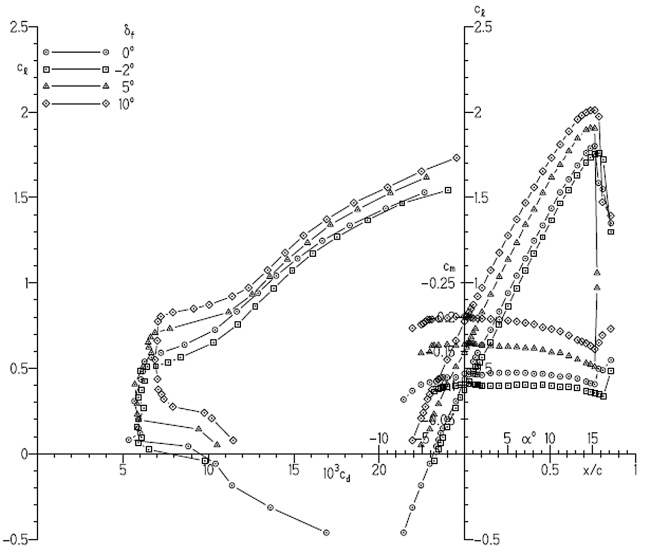

Fig. 8 Effect of flap deflection on section characteristics for $Re_c = 1.00 \times 10^6$ and $M = 0.10$ with transition free.

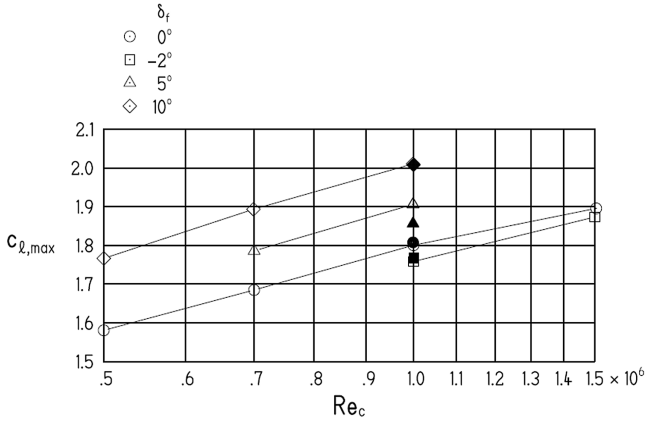

Fig. 9 Variation of maximum lift coefficient with Reynolds number for various flap deflections. Open symbols represent transition free; solid symbols represent transition fixed on the fore element.

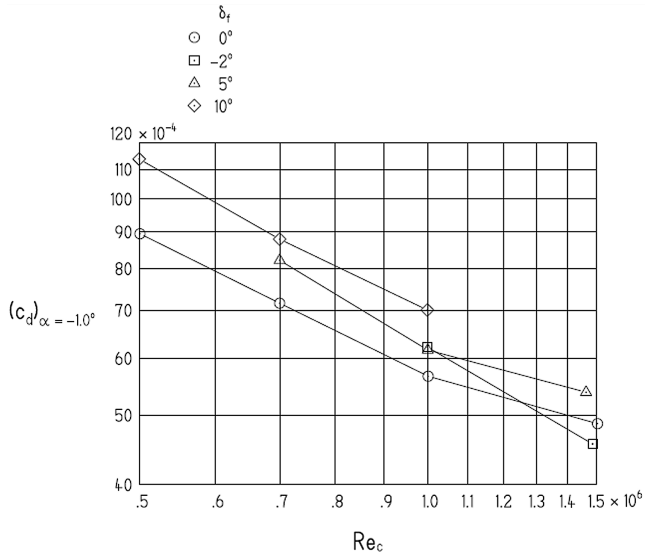

Fig. 10 Variation of profile drag coefficient at $\alpha = 1.02°$ with Reynolds number for various flap deflections.

1.00×10^6, a Mach number of 0.10, and a flap deflection of $-2°$, the lower limit of the low-drag range is shifted downward from that for the 0° flap deflection to about 0.14, which is lower than the design objective of 0.20. The upper limit is about 0.46, which is higher than the objective of 0.30. The maximum lift coefficient is also lower than that with a flap deflection of 0°, and the magnitude of the pitching-moment coefficient at the lower limit of the low-drag range is about 14% smaller. All these results are typical of negative flap deflections.

For the section characteristics with a flap deflection of 10° and transition free, the maximum lift coefficient, the drag coefficients, and the magnitude of the pitching-moment coefficients are higher than those for the smaller flap deflections. All these results are typical of positive flap deflections. For a Reynolds number of 1.00×10^6 and a Mach number of 0.10, the maximum lift coefficient is 2.01, which meets the design objective of 2.00, although it falls short at lower Reynolds numbers.

The variations of maximum lift coefficient and profile-drag coefficient at an angle of attack of $-10°$ with Reynolds number are shown in Figs. 9 and 10, respectively. The trends are quite consistent and affirm the quality of the measurements.

V. Comparison of Theoretical and Experimental Results

A. Pressure Distributions

The comparison of the theoretical and experimental pressure distributions at various lift coefficients with a flap deflection of 0° for a Reynolds number of 1.00×10^6 and a Mach number of 0.10 with transition free is shown in Figs. 11a–11c. At a lift coefficient of 0.31, which is near the middle of the low-drag range and presented in Fig. 5a, the agreement between the predicted and measured pressure coefficients is reasonably good, considering the complexity of the configuration and the strong interaction between the fore and aft elements. The pressure gradients are predicted well, although the magnitude of the theoretical pressure coefficients is less than that of the experimental values. In addition, the laminar separation bubble predicted on the upper surface of the aft element is much less apparent in the measured pressure distribution and forward of the measured location. The discrepancies are in some part due to the slight difference in the zero-lift angle of attack measured in the wind tunnel and that predicted computationally. In addition, a part of this discrepancy is likely due to the disturbances introduced by the plastic film that covers the flap hinge gap in this region.

At a lift coefficient of 1.04, which is roughly halfway between the middle of the low-drag range and the measured maximum lift coefficient and shown in Fig. 5b, the agreement between the predicted and measured pressure coefficients is less precise. Although the pressure gradients are again predicted well, the disparity in the magnitude of the pressure coefficients is greater. The location of the predicted laminar separation bubble on the upper surface of the fore element is aft of the measured location. The laminar separation bubble predicted on the upper surface of the aft element is essentially indistinguishable in the measured pressure distribution.

At a lift coefficient of 1.80, which is the measured maximum lift coefficient and presented in Fig. 5c, the agreement between the predicted and measured pressure coefficients is again less precise and includes disparities in the pressure gradients as well as the magnitude of the pressure coefficients. The location of the laminar separation bubble on the upper surface of the fore element is predicted well, but that of the bubble on the upper surface of the aft element is aft of the measured location.

B. Section Characteristics

The comparison of the theoretical and experimental section characteristics with a flap deflection of 0° and transition free is shown in Fig. 12. The other flap-deflection cases are included in Ref. [24]. In general, the method of Ref. [16] overpredicts the maximum lift coefficient, the lift-curve slope, the drag coefficients within the low-drag range, the lower limit and especially the upper limit of the low-drag range, and the magnitude of the pitching-moment coefficients [26]. The overprediction of the maximum lift coefficient decreases from 13% for a Reynolds number of 0.50×10^6 to 10% for a Reynolds number of 1.50×10^6. The method underpredicts the magnitude of the zero-lift angle and the sharpness of the stall characteristics. The method also fails to capture the large, nose-down pitching-moment coefficient that occurs at stall. Overall, however, the agreement is reasonably good, especially considering the complexity of the configuration.

VI. Conclusions

A 12.91%-thick, flapped, SNLF airfoil, the S702, intended for a low-speed, fixed-wing aircraft, has been designed and analyzed theoretically and verified experimentally in The Pennsylvania State University Low-Speed, Low-Turbulence Wind Tunnel. The two primary objectives of high maximum lift coefficient, insensitive to leading-edge roughness, and low profile-drag coefficients have been achieved. The stall characteristics are sharp but an improvement on the abrupt stall characteristics of earlier SNLF airfoils, which meets the design objective. The constraint on the pitching-moment coefficient has been satisfied. Comparisons of the theoretical and experimental results show reasonably good agreement overall, given the complexity of the configuration.

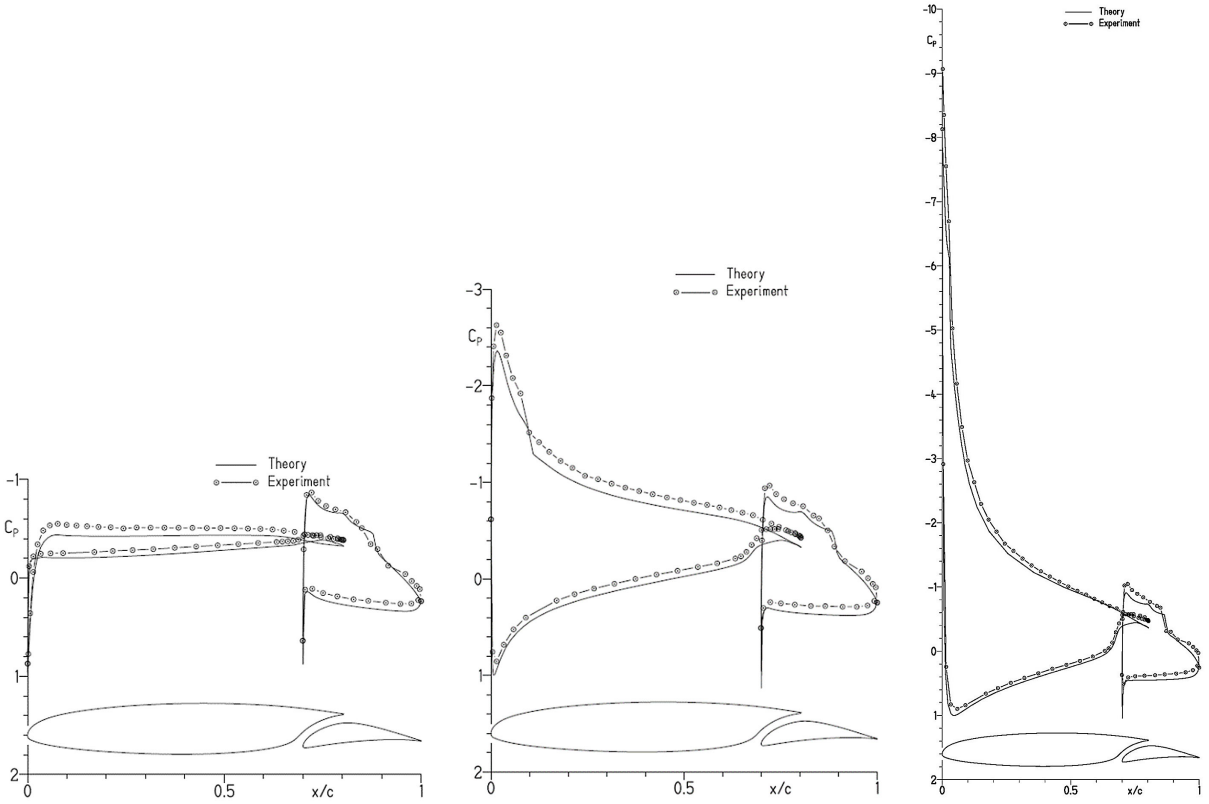

a) $c_l = 0.31$ b) $c_l = 1.04$ c) $c_l = 1.80$

Fig. 11 a–c) Comparison of theoretical and experimental pressure distributions with $\delta_f = 0°$ for $Re_c = 1.00 \times 10^6$ and $M = 0.10$ with transition free.

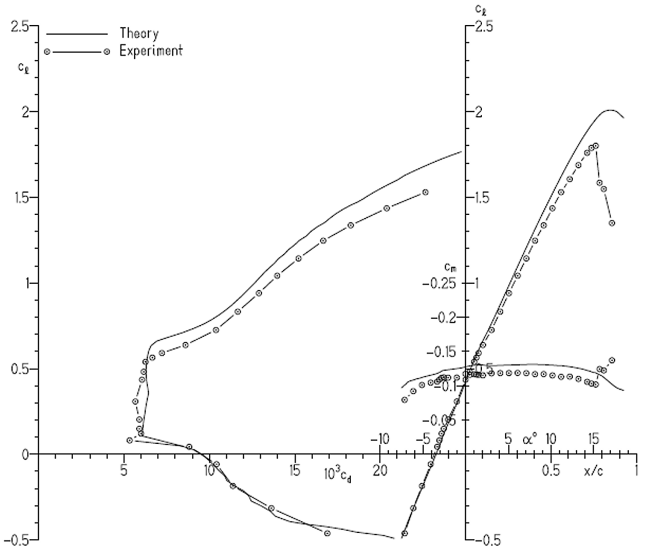

Fig. 12 Comparison of theoretical and experimental section characteristics with $\delta_f = 0°$ and transition free for $Re_c = 1.00 \times 10^6$ and $M = 0.10$.

Acknowledgment

The wind-tunnel model of the S702 airfoil was funded by the University of Tennessee as part of their Cooperative Agreement with the National Aeronautics and Space Administration (NASA) under the University Leadership Initiative (ULI) "Advanced Aerodynamic Design Center for Ultra-Efficient Commercial Vehicles" (Award NNX17AJ95A).

References

[1] Maughmer, M. D., and Somers, D. M., "Figures of Merit for Airfoil/Aircraft Design Integration," AIAA Paper 88-4416, Sept. 1988. https://doi.org/10.2514/MADO88.

[2] Smith, A. M. O., "High-Lift Aerodynamics," *Journal of Aircraft*, Vol. 12, No. 6, 1975, pp. 501–530. https://doi.org/10.2514/3.59830

[3] Jacobs, E. N., "Preliminary Report on Laminar-Flow Airfoils and New Methods Adopted for Airfoil and Boundary Layer Investigations," NACA WR L-345, 1939 (formerly, NACA ACR).

[4] Pfenninger, W., "Investigations on Reductions of Friction on Wings, in Particular by Means of Boundary Layer Suction," NACA TM 1181, 1947*(translated from Mitteilungen aus dem Institut für Aerodynamik an der Eidgenössischen Technischen Hochschule Zürich, Nr. 13*, 1946).

[5] Sudhi, A., Elham, A., and Badrya, C., "Coupled Boundary-Layer Suction and Airfoil Optimization for Hybrid Laminar Flow Control," *AIAA Journal*, Vol. 59, No. 12, Sept. 2021, pp. 5158–5173. https://doi.org/10.2514/1.J060480

[6] Sudhi, A., Radespiel, R., and Badrya, C., "Design Exploration of Transonic Airfoils for Natural and Hybrid Laminar Flow Control Applications," *Journal of Aircraft*, Vol. 60, No. 3, 2023, pp. 716–732. https://doi.org/10.2514/1.C036968

[7] Somers, D. M., "Laminar-Flow Airfoil," U.S. Patent 6,905,092 B2, June 2005.

[8] Coder, J. G., Maughmer, M. D., and Somers, D. M., "Theoretical and Experimental Results for the S414, Slotted, Natural-Laminar-Flow Airfoil," *Journal of Aircraft*, Vol. 51, No. 6, 2014, pp. 1883–1890. https://doi.org/10.2514/1.C032566

[9] Whitcomb, R. T., and Clark, L. R., "An Airfoil Shape for Efficient Flight at Supercritical Mach Numbers," NASA TM X-1109, 1965.

[10] Somers, Dan M., "An Exploratory Investigation of a Slotted, Natural-Laminar-Flow Airfoil," NASA CR-2012-217560, 2012.

[11] Maughmer, M. D., and Somers, D. M., "Design and Experimental Results for a High-Altitude, Long-Endurance Airfoil," *Journal of Aircraft*, Vol. 26, No. 2, 1989, pp. 148–153. https://doi.org/10.2514/3.45736

[12] Eppler, R., "Laminar Airfoils for Reynolds Numbers Greater Than 4×10^6," B-819-35, April 1969. (Available from NTIS as N69-28178; translated from Ingenieur-Archiv, Bd. 38, Heft 4/5, 1969, S. 232–240).

[13] Maughmer, M. D., "Trailing Edge Flow Conditions as a Factor in Airfoil Design," Ph.D. Dissertation, Univ. of Illinois, Champaign, IL, 1983.

[14] Eppler, R., *Airfoil Design and Data*, Springer–Verlag, Berlin, 1990, Chaps. 3 and 5.

[15] Eppler, R., *Airfoil Program System PROFIL11, User's Guide*, Richard Eppler, Stuttgart, Germany, 2011.

[16] Drela, M., "Design and Optimization Method for Multi-Element Airfoils," AIAA Paper 1993-0969, Feb. 1993. https://doi.org/10.2514/6.1993-969

[17] Görtler, H., "On the Three-Dimensional Instability of Laminar Boundary Layers on Concave Walls," NACA TM1375, 1954.

[18] Axten, C. J., and Maughmer, M. D., "An Investigation of Goertler Vortices on Slotted, Natural-Laminar-Flow Airfoils," *AIAA Aviation Forum*, AIAA Paper 2021-2588, Aug. 2021 10.2514/6.2021-2588

[19] Premi, A., Maughmer, M. D., and Brophy, C., "Flow-Quality Measurements and Qualification of the Penn State University Low-Speed, Low-Turbulence Wind Tunnel," AIAA Paper 2012-1214, Jan. 2012. https://doi.org/10.2514/6.2012-1214

[20] Althaus, D., and Eppler, R., "Airfoils with a New Hinge for Ailerons and Flaps," *Motorless Flight Research*, 1972, NASA CR-2315, 1973, pp. 205–217.

[21] Pankhurst, R. C., and Holder, D. W., "Wind-Tunnel Technique," Sir Isaac Pitman & Sons, London, 1965, pp. 270–283.

[22] Allen, H. J., and Vincenti, W. G., "Wall Interference in a Two-Dimensional-Flow Wind Tunnel, with Consideration of the Effect of Compressibility," NACA TR 782, 1944.

[23] "Standard: Assessment of Experimental Uncertainty with Application to Wind-Tunnel Testing," AIAA Paper S-071A-1999, 1999. https://doi.org/10.2514/4.473647.001

[24] Somers, D. M., and Maughmer, M. D., "Design and Experimental Results for a Slotted, Natural-Laminar-Flow Airfoil," NASA CR-20220014964, Dec. 2022.

[25] Loving, D. L., and Katzoff, S., "The Fluorescent-Oil Film Method and Other Techniques for Boundary-Layer Flow Visualization," NASA TM 3-17-59L, 1959.

[26] Coder, J. G., and Maughmer, M. D., "Comparisons of Theoretical Methods for Predicting Airfoil Aerodynamic Characteristics," *Journal of Aircraft*, Vol. 51, No. 1, 2014, pp. 183–191. https://doi.org/10.2514/1.C032232

A. Gopalarathnam
Associate Editor